

# **Aquarius CAP Algorithm and Data User Guide**

*Version: 4.0*

*Simon Yueh, Wenqing Tang, Alexander Fore, and Akiko Hayashi*

*Jet Propulsion Laboratory*

*California Institute of Technology*

*Date: September 20, 2015*

### *Contributors*

The Aquarius geophysical model functions for the CAP algorithm were developed by Dr. Wenqing Tang; the operational setup and processing of the CAP algorithm was completed by Dr. Alex Fore; the setup of data portal and data transfer was performed by Mrs. Akiko Hayashi.

## Document Change Log

<b>Date</b>	<i>Page Numbers</i>	<b>Version</b>	<b>Changes/Comments</b>
February 20, 2013	Page 8	2.0	Updated the cost function by adding two additional terms to constrain the wind speed and direction retrieval
February 20, 2013	Page 11	2.0	Add 10 to the flag to indicate possible rain contamination
February 20, 2013	Pages 5 and 6	2.0	Include the significant wave height as a modeling parameter for radar backscatter and excess emissivity
June 20, 2014	All	3.0	Include the rain corrections to GMFs of radar backscatter and excess emissivity and provide references to the articles on product validation results.
Sept. 20, 2015	Page 6, 8-11, 13-27	4.0	Include the rain corrections to GMFs of excess emissivity with rain-induced near surface stratification accounted for by the Rain Impact Model; and provide results of validation in comparison with APDRC Argo-gridded product and in situ data from moored buoys.

## Contents

I. Purpose .....	4
II. Introduction .....	5
III. Overview of CAP algorithm.....	6
IV. Rain Correction .....	7
V. Validation .....	9
VI. CAP L2 Data and Format .....	13
A. File name convention.....	13
B. Description of datasets in HDF.....	13
1) CAP outputs .....	13
2) Carryover from Aquarius L2 files .....	14
VII. CAP L3 Data and Format .....	15
VIII. References.....	15
IX. Figures and captions .....	18
X. Appendix .....	25

## I. PURPOSE

This document provides an overview of the Combined Active-Passive (CAP) Algorithm for the sea surface roughness correction to enable the retrieval of sea surface salinity, wind speed and direction from Aquarius data. The results from the CAP algorithm are output to files in HDF5 format. This document describes the datasets in the files and their format.

## II. INTRODUCTION

The measurement principle for salinity remote sensing is based on the response of the L-band (1.413 GHz) sea surface brightness temperatures ( $T_B$ ) to sea surface salinity [1]. The influence of wind speed on L-band  $T_B$  has been shown to be about 0.2 to 0.3 K for one  $\text{m.s}^{-1}$  change in wind speed by many field studies [2-7]. To achieve the required 0.2 practical salinity unit (psu) accuracy for Aquarius mission, the impact of sea surface roughness (e.g. wind-generated ripples, foam, and swells) on the observed brightness temperature has to be accurately corrected, ideally to better than one tenth of a degree Kelvin.

The Aquarius radiometer and scatterometer have been fully operating since August 25, 2011. Other than the interruptions caused by a few spacecraft maneuvers, the data acquisition has been continuous. The Aquarius instrument has three antenna beams, operating at about 29, 38 and 46 degrees [8]. Each antenna beam has one radiometer (1.413 GHz), which can acquire the first three Stokes parameters of microwave radiation. The antenna feeds are shared with the scatterometer (1.26 GHz), which acquire the normalized radar cross sections ( $\sigma_0$ ) for co- and cross-polarizations, including VV, HH, VH and HV polarizations.

The Aquarius radiometers make partial polarimetric measurements for the first three Stokes parameters, I, Q, and U [9]. I and Q correspond to the sum and difference of the vertically polarized brightness temperature ( $T_{BV}$ ) and horizontally polarized brightness temperature ( $T_{BH}$ ).  $T_{BV}$  and  $T_{BH}$  are measures of the power of the vertically polarized electrical field ( $E_V$ ) and horizontally polarized electric field ( $E_H$ ), while the third and fourth Stokes parameters (U and V) signify the correlation between  $E_V$  and  $E_H$ :

$$\begin{bmatrix} I \\ Q \\ U \\ V \end{bmatrix} = \begin{bmatrix} T_{BV} + T_{BH} \\ T_{BV} - T_{BH} \\ U \\ V \end{bmatrix} \propto \begin{bmatrix} \langle |E_V|^2 \rangle + \langle |E_H|^2 \rangle \\ \langle |E_V|^2 \rangle - \langle |E_H|^2 \rangle \\ 2 \text{Re} \langle E_V E_H^* \rangle \\ 2 \text{Im} \langle E_V E_H^* \rangle \end{bmatrix} \quad (1)$$

The angular brackets denote the ensemble average of the enclosed quantities. Aquarius does not measure the fourth Stokes V.

The matchup data using either SSM/I or NCEP wind for binning have been used to develop the geophysical model functions (GMF) for Aquarius [13], which relate the microwave backscatter or excess surface emissivity to the wind speed ( $w$ ) and direction ( $\phi$ ). In addition, we include the NOAA WaveWatch-III Significant Wave Height (SWH) to develop the GMF and as ancillary for retrieval. We use the following cosine series for the modeling of radar data:

$$\sigma_{VV}(w, \phi, SWH) = A_{0VV}(w, SWH)[1 + A_{1VV}(w)\cos\phi + A_{2VV}(w)\cos 2\phi] \quad (2)$$

$$\sigma_{HH}(w, \phi, SWH) = A_{0HH}(w, SWH)[1 + A_{1HH}(w)\cos\phi + A_{2HH}(w)\cos 2\phi] \quad (3)$$

Here  $\sigma_{VV}$  and  $\sigma_{HH}$  are the normalized radar backscatter cross-sections for V-transmit/V-receive and H-transmit/H-receive, respectively. The modeling coefficients in Eqs. (2) and (3) are illustrated in [13, 20].

For the radiometer model function, we use the following expressions to characterize the dependence of excess surface emissivity on wind speed, wind direction and SWH:

$$\Delta e_V(w, \phi, SWH) = e_{V0}(w, SWH) + e_{V1}(w) \cos \phi + e_{V2}(w) \cos 2\phi \quad (4)$$

$$\Delta e_H(w, \phi, SWH) = e_{H0}(w, SWH) + e_{H1}(w) \cos \phi + e_{H2}(w) \cos 2\phi \quad (5)$$

$$U(w, \phi) = U_1(w) \sin \phi + U_2(w) \sin 2\phi \quad (6)$$

The third Stokes parameter for the L-band frequency is modeled by the sine function of the wind direction. The modeling coefficients for  $\Delta e_V$  and  $\Delta e_H$  are illustrated in [13, 20].

Given the GMF for excess surface emissivity, following are the complete descriptions of the radiometer model function, which relates the brightness temperatures to surface salinity (SSS), SST, wind speed, wind direction and SWH:

$$T_{BV}(SSS, SST, w, \phi, SWH) = T_{BVflat}(SSS, SST) + SST \cdot \Delta e_{BV}(w, \phi, SWH) \quad (7)$$

$$T_{BH}(SSS, SST, w, \phi, SWH) = T_{BHflat}(SSS, SST) + SST \cdot \Delta e_{BH}(w, \phi, SWH) \quad (8)$$

$$U(SSS, SST, w, \phi) = U_1(w) \sin \phi + U_2(w) \sin 2\phi \quad (9)$$

$T_{Bflat}$  is the brightness temperature for flat water surfaces computed using the water dielectric constant model [10, 11, 16, 20] for given Reynolds SST and SSS. The subscript “p” stands for the polarization. The impact of ocean waves on L-band brightness temperatures and backscatter from the ocean surface was analyzed in [23].

### III. OVERVIEW OF CAP ALGORITHM

The CAP algorithm retrieves the salinity and wind simultaneously by finding the best-fit solution to minimize the difference between the Aquarius data and the model functions described in Eqs. (2)-(9). The earlier versions of the CAP algorithm [12, 13] use different functional forms for the cost function. After gaining more knowledge about the characteristics of the Aquarius L-band microwave data, particularly the weak response of radar backscatter to wind speed near the crosswind direction, we included the last two additional terms in Eq. (10) to constrain the wind speed and direction solutions primarily for near the crosswind directions. Detailed description of the CAP V3.0 retrieval algorithm is provided in [20]. The major updates to V2.0 include improved correction of reflected galactic radiation, geophysical model functions and cost function. The cost function for the CAP Version 3 and 4 algorithm is

$$F_{cap}(SSS, w, \phi) = \sum_{p=V,H} \frac{(T_{Bp} - T_{Bpm})^2}{\Delta T^2} + \sum_{p=V,H} \frac{(\sigma_{0p} - \sigma_{0pm})^2}{(\gamma_p \sigma_{0p})^2} + \frac{(w - w_{NCEP})^2}{\Delta w^2} + \frac{\sin^2[(\phi - \phi_{NCEP})/2]}{\delta^2} \quad (10)$$

The weighting factors for the Aquarius data are set according to the expected measurement and modeling uncertainties. We let  $\Delta T$  be the Noise-Equivalent-Delta-T (NEDT) of radiometer and  $\gamma_p$  be 1.4 times of the radar measurement sensitivity ( $k_{pc}$ ). The values of NEDT and  $k_{pc}$ , a function of signal-to-noise ratio, have been pre-computed and saved in the Aquarius L2 data files. The value of  $\Delta w$  is  $1.5 \text{ ms}^{-1}$ , a rather weak constraint because the accuracy of CAP wind speeds is estimated to be about  $0.7 \text{ ms}^{-1}$  [13]. The value of  $\delta$  is 0.2, which will constrain the wind direction to be within an RMS deviation of 11 degrees from the NCEP wind direction. Our previous analysis [13] indicates that the directional accuracy of the CAP algorithm is about 10 degrees or better for wind speeds of  $15 \text{ ms}^{-1}$  or above. The effect of the last term will not impact the accuracy of the CAP wind direction retrieval for high winds, but will help constrain the wind direction solution for low winds, for which the L-band data have a weak response to wind direction.

For the Aquarius data, we applied the conjugate gradient technique using a modified Levenberg-Marquardt algorithm [14] to find the local minima of  $F_{cap+}$ . There are in general four local minima (ambiguous solutions). This is due to the expansion of the model function for wind direction by including up to the second harmonics of the cosine series. For each given wind speed solution, there will in general be four direction solutions, except when the relative wind direction is along upwind, or downwind or crosswind. This can be easily understood by considering the special case when the  $A_1$  coefficients are zero in the model functions. If the first harmonic coefficient  $A_1$  is zero, these four solutions, corresponding to the inversion of  $\cos 2\phi$ , are  $\phi$ ,  $-\phi$ ,  $\phi + 180^\circ$  and  $180^\circ - \phi$ . If  $A_1$  and  $e_{B1}$  are small, then the third and fourth solutions will shift slightly away from  $\pm \phi + 180^\circ$ . Note that because the cosine series are even functions, the solution pair,  $\pm \phi$ , will produce identical values for model functions, and consequently lead to the same SSS and wind speed solutions. The same is true for the  $\pm \phi + 180^\circ$  solution pair.

A nominal technique developed for the current or past spaceborne wind scatterometer and radiometer missions is the use of numerical weather analysis, such as NCEP or European Center for Medium Range Forecasts (ECMWF), or special wind features to assist the selection of solutions [15]. For salinity and wind speed retrievals, the discrimination of ambiguities is a less challenging issue than ocean wind scatterometers or radiometers because what is needed is to separate the four solutions into two pairs,  $\pm \phi$  and  $\pm \phi + 180^\circ$ , which are separated by about 180 degrees. As previously discussed, each pair will have the same SSS and wind speed values. In our analysis, we use the numerical wind analyses to select the solution by selecting the solution with the closest wind direction to NCEP.

#### IV. RAIN CORRECTION

Based on the analysis of the L-band radiometer/radar residual signals under rainy conditions after accounting for roughness due to wind and flat surface emissivity [16], we introduced a rain correction term for radar/radiometer GMF. For radar backscatter, we have



$$\sigma_{0,p}(w, \phi, SWH, RR) = \sigma_{0,p}^{norain}(w, \phi, SWH) + \sigma_{0,p}^{rain}(w, RR) \quad (11)$$

where  $\sigma_{0,p}^{norain}$  is given by Eqs. (2) & (3) (with  $p$  denotes VV or HH). The rain correction term  $\sigma_{0,p}^{rain}$  is modeled empirically by binning the difference between measured  $\sigma_{0,p}$  and  $\sigma_{0,p}^{norain}$  as a function of surface rain rate (RR) and wind speed ( $w$ ).

Similarly for radiometer, we have,

$$\Delta e_p(w, \phi, SWH, RR) = \Delta e_p^{norain}(w, \phi, SWH) + \Delta e_p^{rain}(w, RR) \quad (12)$$

where  $\Delta e_p^{norain}$  is given by Eqs. (4) & (5) for V-pol and H-pol respectively. The rain correction term  $\Delta e_p^{rain}$  is modeled from binning the difference between measured brightness temperature and  $\Delta e_p^{norain}$ , with emissivity from the flat surface calculated from the sea surface temperature (SST) [17] and  $SSS_{RIM}$ , which is HYCOM SSS [18] adjusted by a rain impact model [24, 25] to account for the rain effect on the near surface salinity stratification [26]. HYCOM assimilates the ocean surface's space-time variability on SST and SSH (sea surface height) obtained from satellite observations, the salinity information assimilated is from profiling floats, e.g. ARGO, which mainly operate at 5 meters below the surface. Therefore HYCOM SSS does not represent the first centimeter or skin salinity, rather the bulk salinity in the upper few meters. Under persistently rainy conditions, there are often near surface stratification. Hence it is expected that the rain-dilution effect on HYCOM SSS will be reduced with respect to the effect on the salinity sampled by the radiometer at 1-2 cm depth [21]. When calibrated with  $SSS_{RIM}$ , the residuals, i.e. the difference between measured and model predicted brightness temperature  $T_B$ , are considered as rain-induced roughness. It was found that rain-induced roughness is larger at lower wind speeds, and decreases as wind increases. The Combined Active Passive algorithm is used to retrieve SSS with ( $SSS_{CAP\_RC}$ ) or without ( $SSS_{CAP}$ ) rain roughness correction. We find that the simultaneously retrieved wind speed with rain roughness correction has significantly improved agreement with the NCEP wind speed with the rain-dependent bias reduced, justifying our rain correction approach. SSS retrieved is validated with salinity measured by drifters at a depth of 45cm. The difference between satellite retrieved and in situ salinity increases with rain rate. With rain-induced roughness accounted for, the difference between satellite retrieval and drifter increases with rain rate with slope of  $-0.184 \text{ psu (mm hr}^{-1})^{-1}$ , representing the salinity stratification between the two depths (1-2 cm vs. 45 cm).

The ancillary rain rate data used for previous versions of CAP retrieval were based on SSMI/S or WindSAT measurements. With the collocation criteria of one hour and 12.5 km radius, the combined SSMI/S and WindSAT covers about 80% of Aquarius level 2 data blocks. In this version of CAP retrieval, we replaced the ancillary rain rate with matchups based on NOAA CMORPH rain rates at resolution of  $0.25^\circ$  and 30 minutes [27, 28]. The morphing method uses motion vectors derived from half-hourly interval geostationary satellite infrared (IR) imagery to propagate precipitation estimates derived from multiple instruments. The constellation of microwave passive radiometer includes concurrent DMSP SSM/I and SSMI/S, the NOAA AMSU-B, GCOM-W AMSR-2 and TRMM TMI. The high temporal resolution of CMORPH rain rate ensures each Aquarius level 2 data block associated with a valid rain rate matchup,

## V. VALIDATION

The accuracy of the previous version of CAP retrieval was assessed for wind [19] and salinity [21, 22]. This report documents the validation results for CAP V4.0 salinity.

To validate level 3 CAP salinity data, the monthly Argo [29] gridded data was obtained from the Asia-Pacific Data-Research Center (APDRC) of the International Pacific Research Center (IPRC) at the University of Hawaii (available from <http://apdrc.soest.hawaii.edu>). Figure 1 shows the difference between CAP retrieval and APDRC Argo. One of the main difference patterns is the zonally orientated narrow bands of negative values of satellite minus APDRC Argo (blue), for example, in the Pacific Inter tropical convergence zone (ITCZ). As discussed in [22], this may be associated with the surface freshening from rainfall captured by Aquarius while missed by Argo floats a few meters below the surface. On the other hand, Aquarius SSS have a positive bias throughout the year in the high latitude (pole-ward of  $40^\circ$ ), where larger satellite measurement error is expected due to loss of the salinity signal in emissivity in cold water, as well as fewer number of available samples from Argo floats in these regions. Between  $40^\circ\text{S}$  and  $40^\circ\text{N}$ , the bias with respect to APDRC Argo is less than 0.05 PSU for all months, with RMS difference less than 0.2 PSU (Fig. 2).

Although Argo is the best available source with consistent global coverage that can be used to assess Aquarius SSS performance, it may not be sufficient to depict processes with rapid temporal variability. Moreover, the shallowest depth where Argo floats can operate reliably is 5-meters below the surface, where salinity may largely differ from that from Aquarius in regions with high near surface stratification. On the other hand, the moored buoys provide daily salinity measurements at 1-meter depth, which provide measurements nearer to the surface and with higher temporal sampling [30,31,32]. However, buoy locations are sparse and the data records at each position may be discontinuous.

We downloaded the time series of daily salinity measured at 1-m depth by TAO/PIRATA/RAMA moored buoys from [www.pmel.noaa.gov/tao](http://www.pmel.noaa.gov/tao). The Aquarius SSS daily records are created using all available Level 2 data blocks within 111 km from the buoy location and averaged using Gaussian weighting with half-power distance of 75 km (similar to the Level 3 gridding), only if there are more than 20 data blocks collocated. The Aquarius local sampling interval varies by location, with at least one daily sample every 7 days in the tropics. To be consistent with Level 3 monthly data validation, a 30-day moving average is applied to the time series of each product at each buoy location. The time series of APDRC Argo at each buoy location is created in the same way from Argo matchups with Aquarius Level 2 data blocks obtained using spatial and temporal interpolation from APDRC Argo monthly gridded data. As examples, Fig. 3 illustrated the 30-day moving averaged daily time series at two buoy locations: in the western Pacific warm pool at TAO buoy located at  $156^\circ\text{E}$  on the Equator (Fig.3a), and in the Indian Ocean at RAMA buoy located at  $5^\circ\text{S}$ ,  $95^\circ\text{E}$  (Fig.3b). The time series of HYCOM and APDRC Argo are also over-plotted for comparison. Figure 4 shows color-coded correlation coefficient, bias and RMS difference between buoy 1-m salinity and  $\text{SSS}_{\text{CAP}}$  &  $\text{SSS}_{\text{CAP\_RC}}$  over the entire buoy array. The statistical values at each buoy location are listed in Table 1, with corresponding time series plot given in Appendix A. Table 2 gives values of bias, RMSD and correlation coefficients averaged over all the buoys. The CAP SSS with or without rain

correction has an excellent agreement with the buoy data with the RMSD reaching about 0.14 psu.

Table 1. Comparison of SSS<sub>CAP</sub>, SSS<sub>CAP\_RC</sub>, SSS<sub>HYCOM</sub>, and APDRC Argo with 1-m salinity observed daily by in situ moored buoy. Biases, RMS differences and correlation coefficients are provided at each buoy location. N indicates the number of available buoy 1-m salinity daily records between September 1, 2011 and May 31, 2015. Time series plots at each buoy location are given in Appendix A in the same order of the Table list.

Station	N	Bias (-buoy) [PSU]				RMS difference [PSU]				Correlation Coefficients			
		CAP	CAP_RC	HYCOM	APDRC	CAP	CAP_RC	HYCOM	APDRC	CAP	CAP_RC	HYCOM	APDRC
s0n0e	598	0.023	0.031	-0.008	0.184	0.197	0.196	0.302	0.371	0.920	0.922	0.802	0.801
s0n10w	865	0.356	0.347	0.218	0.099	0.437	0.424	0.399	0.391	0.869	0.876	0.742	0.655
s0n110w	646	-0.022	-0.013	0.015	-0.116	0.100	0.095	0.171	0.192	0.941	0.946	0.825	0.852
s0n125w	545	-0.008	-0.006	-0.044	-0.059	0.084	0.085	0.182	0.169	0.938	0.935	0.762	0.806
s0n137e	526	0.133	0.151	0.176	-0.036	0.225	0.236	0.242	0.259	0.845	0.845	0.960	0.645
s0n140w	407	0.014	0.014	-0.003	-0.058	0.083	0.083	0.107	0.117	0.737	0.737	0.480	0.535
s0n147e	1321	0.090	0.112	0.190	0.020	0.177	0.182	0.252	0.179	0.906	0.909	0.940	0.866
s0n155w	509	0.108	0.109	-0.012	-0.047	0.136	0.137	0.076	0.083	0.650	0.654	0.685	0.759
s0n156e	1263	-0.016	-0.007	0.075	-0.065	0.100	0.103	0.222	0.270	0.979	0.977	0.913	0.849
s0n165e	290	0.041	0.036	0.049	-0.024	0.104	0.113	0.171	0.180	0.975	0.970	0.959	0.960
s0n170w	1121	0.083	0.088	-0.090	-0.098	0.120	0.120	0.122	0.135	0.544	0.586	0.538	0.479
s0n180w	607	0.077	0.079	-0.022	-0.105	0.114	0.116	0.136	0.133	0.887	0.882	0.653	0.887
s0n23w	1171	0.064	0.070	0.019	-0.210	0.116	0.122	0.158	0.301	0.904	0.894	0.754	0.292
s0n35w	614	0.018	0.020	-0.074	-0.301	0.103	0.112	0.138	0.344	0.808	0.779	0.676	0.507
s0n67e	298	0.013	0.019	0.033	0.062	0.090	0.092	0.083	0.141	0.933	0.931	0.974	0.857
s0n90e	510	-0.004	0.007	0.097	-0.003	0.150	0.150	0.167	0.133	0.844	0.835	0.813	0.833
s0n95w	666	0.025	0.031	0.072	-0.133	0.223	0.225	0.340	0.292	0.885	0.885	0.716	0.882
s10s10w	1044	0.156	0.156	-0.002	0.017	0.194	0.194	0.155	0.149	0.813	0.814	0.631	0.685
s12n23w	688	0.142	0.142	0.089	0.098	0.177	0.177	0.132	0.141	0.903	0.901	0.918	0.929
s12n38w	433	0.111	0.111	0.123	0.165	0.216	0.220	0.255	0.306	0.796	0.783	0.685	0.602
s12n90e	710	-0.053	-0.050	-0.003	-0.204	0.297	0.296	0.384	0.418	0.846	0.847	0.680	0.735
s12s55e	1079	0.030	0.027	-0.046	0.020	0.140	0.141	0.101	0.111	0.845	0.842	0.911	0.862
s12s67e	838	0.066	0.070	0.063	0.055	0.153	0.146	0.199	0.221	0.940	0.942	0.850	0.769
s12s93e	132	-0.154	-0.142	0.029	-0.031	0.233	0.221	0.200	0.174	0.720	0.740	0.654	0.840
s14s32w	815	0.071	0.071	0.024	0.037	0.123	0.123	0.131	0.121	0.817	0.820	0.592	0.667
s15n38w	1075	0.003	-0.001	-0.024	0.123	0.124	0.131	0.165	0.188	0.749	0.725	0.562	0.685
s15n90e	674	0.080	0.082	0.378	-0.081	0.449	0.441	0.701	0.461	0.756	0.764	0.439	0.726
s16s55e	506	0.082	0.079	-0.046	0.011	0.097	0.094	0.143	0.103	0.970	0.970	0.774	0.869
s19s34w	1227	0.234	0.222	-0.164	-0.011	0.275	0.269	0.204	0.106	0.153	0.193	0.431	0.241
s20n38w	541	0.054	0.055	0.085	0.187	0.139	0.139	0.146	0.223	0.466	0.466	0.397	0.187
s21n23w	1078	0.189	0.189	0.066	0.238	0.243	0.242	0.175	0.294	0.706	0.705	0.657	0.620
s25s100e	821	0.019	0.017	0.130	-0.012	0.162	0.160	0.183	0.172	0.703	0.712	0.847	0.651
s2n110w	1220	0.008	0.012	0.050	0.008	0.172	0.186	0.240	0.212	0.858	0.835	0.696	0.805
s2n125w	745	-0.013	-0.000	-0.114	-0.056	0.089	0.077	0.193	0.164	0.904	0.927	0.677	0.690
s2n130e	558	0.184	0.197	0.218	-0.137	0.228	0.237	0.276	0.231	0.876	0.872	0.770	0.621
s2n137e	1030	0.109	0.124	0.156	-0.071	0.169	0.177	0.227	0.185	0.906	0.911	0.862	0.857
s2n140w	879	0.037	0.040	-0.013	0.000	0.086	0.087	0.125	0.126	0.839	0.838	0.528	0.524
s2n147e	1265	-0.022	-0.015	0.184	0.024	0.098	0.097	0.241	0.160	0.959	0.958	0.917	0.907
s2n155w	1049	0.022	0.026	-0.043	-0.085	0.095	0.091	0.096	0.128	0.748	0.767	0.758	0.714
s2n156e	1309	-0.021	0.002	0.131	-0.072	0.122	0.116	0.231	0.191	0.946	0.950	0.903	0.895
s2n165e	745	0.169	0.177	0.217	0.103	0.294	0.300	0.401	0.330	0.866	0.866	0.745	0.772
s2n170w	935	0.015	0.014	-0.136	-0.154	0.104	0.101	0.210	0.190	0.842	0.854	0.552	0.812
s2n180w	1075	0.027	0.030	-0.102	-0.167	0.107	0.111	0.194	0.208	0.890	0.883	0.700	0.831
s2n95w	359	-0.084	-0.068	0.242	0.168	0.215	0.209	0.394	0.395	0.932	0.933	0.865	0.787
s2s110w	632	0.027	0.028	0.041	-0.084	0.108	0.109	0.195	0.196	0.943	0.942	0.836	0.843
s2s125w	405	0.050	0.053	-0.068	-0.065	0.098	0.098	0.118	0.106	0.806	0.810	0.638	0.722
s2s140w	929	0.164	0.163	0.038	0.056	0.260	0.259	0.234	0.195	0.437	0.439	0.127	0.548
s2s155w	726	0.072	0.074	-0.027	-0.036	0.104	0.105	0.065	0.058	0.681	0.687	0.795	0.897
s2s156e	1309	-0.051	-0.044	-0.009	-0.188	0.120	0.111	0.196	0.255	0.969	0.971	0.884	0.900
s2s165e	799	-0.193	-0.193	-0.235	-0.286	0.326	0.327	0.315	0.340	0.856	0.852	0.797	0.865
s2s170w	1082	0.052	0.055	-0.129	-0.083	0.098	0.098	0.161	0.105	0.723	0.726	0.613	0.841
s2s180w	481	0.070	0.074	-0.095	-0.050	0.108	0.110	0.139	0.076	0.657	0.651	0.128	0.549
s2s95w	857	0.024	0.032	-0.059	-0.188	0.104	0.103	0.176	0.218	0.959	0.960	0.876	0.951
s4n23w	400	0.078	0.088	0.114	0.105	0.173	0.191	0.211	0.250	0.812	0.762	0.657	0.380
s4n38w	447	-0.053	-0.039	-0.048	-0.190	0.138	0.134	0.174	0.290	0.818	0.811	0.690	0.179
s4n90e	522	-0.101	-0.087	0.141	-0.023	0.232	0.218	0.348	0.416	0.904	0.915	0.852	0.687
s4s67e	518	0.064	0.068	0.032	0.068	0.122	0.123	0.106	0.138	0.856	0.858	0.851	0.792
s5n110w	1026	-0.049	-0.033	-0.082	-0.199	0.149	0.130	0.271	0.374	0.889	0.907	0.503	0.124
s5n125w	724	-0.013	-0.007	-0.086	-0.108	0.133	0.126	0.339	0.373	0.891	0.901	-0.381	-0.148
s5n137e	1059	-0.047	-0.037	0.156	0.022	0.108	0.103	0.232	0.238	0.956	0.958	0.897	0.784

s5n140w	760	0.017	0.021	-0.058	-0.093	0.150	0.148	0.243	0.254	0.759	0.766	0.137	-0.046
s5n147e	887	-0.000	0.007	0.232	0.158	0.096	0.093	0.290	0.268	0.958	0.961	0.899	0.837
s5n155w	1020	-0.036	-0.036	-0.145	-0.213	0.096	0.103	0.245	0.266	0.929	0.925	0.530	0.672
s5n156e	1189	-0.019	-0.002	0.171	0.084	0.102	0.104	0.206	0.168	0.929	0.923	0.891	0.822
s5n165e	985	-0.031	-0.016	0.104	0.032	0.112	0.108	0.175	0.189	0.937	0.938	0.884	0.796
s5n170w	592	0.057	0.058	0.016	0.046	0.256	0.259	0.185	0.208	0.865	0.857	0.840	0.798
s5n180w	302	0.061	0.052	0.037	0.029	0.173	0.165	0.156	0.152	0.941	0.945	0.911	0.901
s5n95w	784	0.041	0.066	0.501	0.428	0.186	0.199	0.668	0.625	0.949	0.946	0.686	0.640
s5s110w	631	0.117	0.119	0.060	0.083	0.194	0.194	0.164	0.208	0.834	0.834	0.885	0.704
s5s125w	954	0.028	0.030	-0.049	-0.048	0.073	0.072	0.202	0.150	0.943	0.947	0.309	0.784
s5s140w	296	0.119	0.120	-0.011	0.044	0.126	0.127	0.049	0.096	0.957	0.958	0.932	0.941
s5s155w	1104	-0.043	-0.044	-0.058	-0.067	0.119	0.121	0.129	0.129	0.614	0.601	0.524	0.636
s5s156e	1179	0.009	0.054	0.034	-0.020	0.208	0.188	0.172	0.135	0.803	0.840	0.823	0.869
s5s165e	366	-0.100	-0.075	-0.300	-0.233	0.162	0.133	0.412	0.305	0.955	0.961	0.116	0.850
s5s170w	641	0.033	0.037	-0.055	-0.028	0.096	0.095	0.103	0.141	0.719	0.730	0.685	0.164
s5s180w	813	0.092	0.102	-0.057	0.030	0.216	0.223	0.151	0.185	0.668	0.664	0.769	0.594
s5s95e	988	-0.060	-0.034	0.100	-0.091	0.166	0.153	0.163	0.189	0.793	0.790	0.767	0.550
s5s95w	691	0.094	0.097	0.021	0.152	0.156	0.156	0.277	0.309	0.961	0.962	0.825	0.892
s6s10w	837	0.058	0.058	-0.032	-0.000	0.113	0.114	0.113	0.147	0.867	0.866	0.832	0.664
s6s8e	356	-0.052	-0.058	-0.123	0.350	0.497	0.505	0.775	0.767	0.900	0.896	0.780	0.880
s8n110w	1211	0.174	0.166	0.364	0.228	0.380	0.376	0.471	0.395	0.724	0.729	0.785	0.785
s8n125w	700	-0.028	-0.028	0.051	-0.002	0.155	0.159	0.219	0.184	0.861	0.852	0.697	0.789
s8n130e	561	0.090	0.102	0.352	0.162	0.161	0.172	0.390	0.203	0.741	0.715	0.504	0.787
s8n137e	1307	0.064	0.077	0.163	0.124	0.113	0.118	0.232	0.193	0.917	0.922	0.733	0.774
s8n155w	709	-0.033	-0.027	0.094	0.065	0.106	0.104	0.188	0.158	0.972	0.972	0.931	0.954
s8n156e	908	0.071	0.082	0.146	0.130	0.146	0.146	0.208	0.177	0.868	0.878	0.827	0.904
s8n165e	706	0.001	0.011	0.228	0.174	0.141	0.136	0.279	0.214	0.712	0.728	0.558	0.786
s8n170w	322	0.027	0.028	0.077	0.105	0.095	0.089	0.268	0.230	0.991	0.993	0.949	0.969
s0n80.5e	686	-0.017	-0.018	0.049	0.004	0.131	0.142	0.138	0.244	0.870	0.847	0.884	0.359
s12s80.5e	1305	0.059	0.062	0.072	0.004	0.162	0.154	0.125	0.150	0.935	0.940	0.949	0.863
s1.5n80.5e	336	0.050	0.056	0.083	0.111	0.382	0.380	0.395	0.497	0.549	0.570	0.632	-0.228
s1.5n90e	225	0.121	0.123	0.326	0.197	0.230	0.245	0.370	0.267	0.871	0.850	0.914	0.896
s1.5s67e	394	0.059	0.069	0.090	0.112	0.114	0.121	0.128	0.206	0.851	0.850	0.840	0.416
s1.5s80.5e	970	0.082	0.081	0.164	0.058	0.174	0.181	0.254	0.173	0.845	0.827	0.749	0.833
s1.5s90e	289	-0.038	-0.039	0.063	-0.002	0.178	0.186	0.141	0.106	0.609	0.601	0.789	0.874
s16s80.5e	536	0.078	0.069	0.052	-0.039	0.167	0.167	0.125	0.131	0.734	0.725	0.778	0.750
s4s80.5e	723	0.035	0.021	0.160	0.041	0.141	0.170	0.254	0.167	0.942	0.915	0.898	0.938
s8s80.5e	1002	-0.079	-0.076	0.167	0.011	0.171	0.168	0.285	0.215	0.962	0.960	0.904	0.893

Table 2. Comparison of  $SSS_{CAP}$ ,  $SSS_{CAP\_RC}$ ,  $SSS_{HYCOM}$ , and APDRC Argo with 1-m salinity observed daily by in situ moored buoy with the values averaged over all the buoys.

	CAP	CAP_RC	HYCOM	APDRC
<b>Bias [PSU]</b>	0.032	0.036	0.043	0.001
<b>RMSD [PSU]</b>	0.141	0.141	0.191	0.190
<b>Correlation</b>	0.710	0.711	0.611	0.600

## VI. CAP L2 DATA AND FORMAT

The Aquarius CAP L2 files contain the CAP algorithm outputs and a few datasets in the Aquarius L2 data files, in HDF format.

### A. File name convention

The file names are similar to the Aquarius L2 files. The first part of the file name is the same as that in the Aquarius L2 files. We added the extension '.cap' to it.

For example, Q2012001012500.L2\_SCI\_V4.0.cap, is the file for the data pass started at 01:25:00 UT on day 1, 2012. "L2\_SCI\_V4.0" indicates the version of Aquarius L2 files used for the CAP processing.

### B. Description of datasets in HDF

The datasets in the HDF5 files are part of the root file, not in a "Aquarius Data" group. Each dataset has 4083 blocks for 3 antenna beams.

A simple way to separate the data from ascending and descending passes for ocean observations is to use the first array index of the dataset. If the first array index is smaller (greater) than 2042, then the data are from ascending (descending) orbits.

#### 1) CAP outputs

The CAP data and critical time and location data sets are outlined below.

Dataset	Size (Block, Beam)	Format	Unit	Valid range	Description
Sec	Dataset {4083}	double float	Seconds	0.d0 to 86399.999999d0	Block time in seconds of day
beam_clat	Dataset {4083, 3}	float	Degree	-90 to 90	Latitude of footprint
beam_clon	Dataset {4083, 3}	float	Degrees	-180 to 180	Longitude of footprint
SSS_cap	Dataset {4083, 3}	float	Psu	0 to 50	SSS from the CAP algorithm
SSS_cap_rc	Dataset {4083,3}	Float	Psu	0 to 50	SSS from the CAP with rain correction if RR>0; SSS_cap_rc is identical to SSS_cap if no rain (RR=0), or there is no rain data matchup with Aquarius

SSS_cap_v	Dataset {4083, 3}	float	Psu	0 to 50	SSS retrieved from the V-pol TB using the scat_wind_speed for excess surface emissivity correction
wind_speed_cap	Dataset {4083, 3}	float	Meters per sec	Greater than 0	Wind speed retrieved from the CAP algorithm
wind_dir_cap	Dataset {4083, 3}	float	Degrees	-180 to 180	Wind direction retrieved from the CAP algorithm
cap_flag	Dataset {4083, 3}	H5T_NA TIME_U CHAR		0 to 5, 10 to 15 and 100*	Flag for CAP retrieval
scat_wind_speed	Dataset {4083, 3}	float	Meters per sec	Greater than 0	Wind speed retrieved from the Aquarius scatterometer data using the NCEP wind direction as ancillary information

wind\_dir\_cap is the wind direction retrieved from the Aquarius data, and is the direction from with respect to the north in clockwise direction. Its error is less than 20 degrees RMS at greater than 12 m/s wind speeds for beam 1 and 10 m/s for beams 2 and 3.

cap\_flag: The flag for CAP algorithm retrieval with the values of 0, 1, and 2 for valid SSS retrieval and 3 and 4 for invalid SSS retrieval. If the matchup rain rate (RR) from SSMIS or WindSat is greater than zero, we add 10 to the flag to indicate possible rain contamination.

- 0 for  $\text{abs}(\text{wind\_speed\_cap} - \text{anc\_wind\_speed}) < 15$  m/s
- 1 for  $\text{abs}(\text{wind\_speed\_cap} - \text{anc\_wind\_speed}) < 30$  m/s
- 2 for  $\text{abs}(\text{wind\_speed\_cap} - \text{anc\_wind\_speed}) > 30$  m/s
- 3 for  $\text{wind\_speed\_cap} < 0$  or  $\text{sss\_cap} < 0$  or  $\text{sss\_cap} > 50$
- 4 for no retrieval
- 5 for  $\text{TB}_{err} \geq 0.4$  K, where  $\text{TB}_{err} = \sqrt{(\text{TB}_V^{\text{meas.}} - \text{TB}_V^{\text{mod.}})^2 + (\text{TB}_H^{\text{meas.}} - \text{TB}_H^{\text{mod.}})^2}$
- 10 for  $\text{abs}(\text{wind\_speed\_cap} - \text{anc\_wind\_speed}) < 15$  m/s and  $\text{RR} > 0$
- 11 for  $\text{abs}(\text{wind\_speed\_cap} - \text{anc\_wind\_speed}) < 30$  m/s and  $\text{RR} > 0$
- 12 for  $\text{abs}(\text{wind\_speed\_cap} - \text{anc\_wind\_speed}) > 30$  m/s and  $\text{RR} > 0$
- 13 for  $\text{wind\_speed\_cap} < 0$  or  $\text{sss\_cap} < 0$  or  $\text{sss\_cap} > 50$  and  $\text{RR} > 0$
- 14 for no retrieval and  $\text{RR} > 0$
- 15 for  $\text{TB}_{err} \geq 0.4$  K and  $\text{RR} > 0$

\*We added 100 to the cap\_flag if  $\text{abs}(\text{rad\_TaV} - \text{rad\_TfV}) \geq 1$  or  $\text{abs}(\text{rad\_TaH} - \text{rad\_TfH}) \geq 1$ .

## 2) Carryover from Aquarius L2 files

The following are datasets carried over from the Aquarius L2 files. They are included for ease of comparison with the CAP products.

Dataset	Size (Block, Beam)	Unit	Description
SSS	Dataset {4083, 3}	Psu	SSS in the Aquarius L2 files
anc_SSS	Dataset {4083, 3}	Psu	Ancillary (HYCOM) SSS in the Aquarius L2 files
anc_surface_temp	Dataset {4083, 3}	Kelvin	SST in the Aquarius L2 files
anc_wind_speed	Dataset {4083, 3}	Meters per sec	Ancillary (NCEP) wind speed in the Aquarius L2 files
anc_wind_dir	Dataset {4083, 3}	Degrees	Ancillary wind direction (NCEP) in the Aquarius L2 files
scat_land_frac	Dataset {4083, 3}		Scatterometer land fraction in the Aquarius L2 files (unitless between 0 and 1)
scat_ice_frac	Dataset {4083, 3}		Scatterometer ice fraction in the Aquarius L2 files (unitless between 0 and 1)
land_frac	Dataset {4083, 3}		Radiometer land fraction in the Aquarius L2 files (unitless between 0 and 1)
ice_frac	Dataset {4083, 3}		Radioemter ice fraction in the Aquarius L2 files (unitless between 0 and 1)

## VII. CAP L3 DATA AND FORMAT

The Aquarius CAP L3 data contain monthly and weekly maps on  $1^\circ \times 1^\circ$  grid for both SSS\_cap and SSS\_cap\_rc, in netcdf format. L3 data are created using Gaussian weighting with half-power and searching distances at 75 and 111 km, respectively. The filtering criteria for transferring data from Level 2 to Level 3 are:  $\text{land\_frac} < 0.01$ ,  $\text{ice\_frac} < 0.0005$ ,  $\text{anc\_surface\_temp} > 273$ , and  $\text{cap\_flag} < 3$  or  $10 \leq \text{cap\_flag} < 13$ , in addition to checking the radiometer flag included in Aquarius L2 files for non-nominal navigation (bit-12), and pointing anomaly (bit-16).

## VIII. REFERENCES

- [1] Yueh, S. H., R. West, W. J. Wilson, F. K. Li, E. G. Njoku, and Y. Rahmat-Samii, "Error sources and feasibility for microwave remote sensing of ocean surface salinity", *IEEE Trans. Geosci. Remote Sensing*, 39, 1049-1060, 2001.
- [2] Hollinger, J. P., "Passive microwave measurements of sea surface roughness", *IEEE Trans. Geosci. Electron.*, vol. GE-9, pp. 165–169, July 1971.
- [3] Camps, A., J. Font, M. Vall-Llossera, C. Gabarro, I. Corbella, N. Duffo, F. Torres, S. Blanch, A. Aguasca, R. Villarino, L. Enrique, J.J. Miranda, J.J. Arenas, A. Juliaa, J. Etcheto, V. Caselles, A. Weill, J. Boutin, S. Contardo, R. Niclos, R. Rivas, S.C. Reising, P. Wursteisen, M. Berger, and M. Martin-Neira, "The WISE 2000 and 2001 field experiments in support of the SMOS mission: Sea surface L-band brightness temperature observations and their application to sea surface salinity retrieval," *IEEE Trans. Geoscience and Remote Sensing*, vol. 42, no. 4, pp. 804-823, April 2004.



- [4] Etcheto, J., E. P. Dinnat, J. Boutin, A. Camps, J. Miller, Stephanie, J. Wesson, J. Font, and D. Long, "Wind speed effect on L-band brightness temperature inferred from EuroSTARRS and WISE 2001 field experiments." Vol. 42, no. 10, pp. 2206-2213, October 2004.
- [5] Gabarro, C. J. Font, A. Camps, M. Vall-Llossera, and A. Julia, "A new empirical model of sea surface microwave emissivity for salinity remote sensing," *Geophysical Research Letters*, vol. 31, no. 1, pp. 5, January 2004.
- [6] Camps, A., M. Vall-Llossera, R. Villarino, N. Reul, B. Chapron, I. Corbella, N. Duffo, F. Torres, J.J. Miranda, R. Sabia, A. Monerris, R. Rodriguez, "The Emissivity of Foam-Covered Water Surface at L-Band: Theoretical Modeling and Experimental Results From the Frog 2003 Field Experiment", *IEEE Trans. Geosci. Remote Sensing*, vol. 43, issue 5, pp. 925-937, May 2005.
- [7] Yueh, S. H., S. Dinardo, A. Fore, and F. Li, "Passive and Active L-Band Microwave Observations and Modeling of Ocean Surface Winds", *IEEE Trans. Geosci. And Remote Sensing*, Vol. 48, No. 8, pp. 3087-3100, August 2010.
- [8] Le Vine, D. M., G.S.E. Lagerloef, R. Coloma, S. Yueh, and F. Pellerano, "Aquarius: An Instrument to Monitor Sea Surface Salinity from Space," *IEEE Trans. Geosci. And Remote Sensing*, Vol. 45, No. 7, 2040-2050, July 2007.
- [9] Kraus, J. D., *Radio Astronomy*, 2nd. ed., 1986, Cygnus-Quasar Books, Powell, Ohio.
- [10] Meissner T. and F. Wentz, "The Complex Dielectric Constant of Pure and Sea Water From Microwave Satellite Observations", *IEEE TGARS*, vol. 42 (9), 1836 – 1849, 2004.
- [11] Klein, L., & C. Swift, "An improved model for the dielectric constant of sea water at microwave frequencies". *IEEE Trans. on Antennas and Propagation*, 25, (1), 104 – 111, 1977.
- [12] Yueh S. and J. Chaubell, "Sea Surface Salinity and Wind Retrieval using Combined Passive and Active L-Band Microwave Observations", *IEEE Trans. Geosci. Remote Sens.*, Vol. 50, No. 4, pp. 1022-1032, April 2012.
- [13] Yueh, S. H., W. Tang, A. Fore, G. Neumann, A. Hayashi, A. Freedman, J. Chaubell, and G. Lagerloef, "L-band Passive and Active Microwave Geophysical Model Functions of Ocean Surface Winds and Applications to Aquarius Retrieval," *IEEE Trans. Geoscience and Remote Sensing*, 51(9), 4619-4632, DOI: 10.1109/TGRS.2013.2266915, 2013.
- [14] Burton, S. Garbow, Kenneth E. Hillstrom, Jorge J. More, Documentation for Minpack, Argonne National Laboratory, <http://www.netlib.org/minpack/>
- [15] Figa-Saldaña, J., J.J.W. Wilson, E. Attema, R. Gelsthorpe, M.R. Drinkwater, and A. Stoffelen, The advanced scatterometer (ASCAT) on the meteorological operational (MetOp) platform: A follow on for European wind scatterometers, *Can. J. Remote Sensing*, Vol. 28, No. 3, pp. 404–412, 2002.
- [16] Tang, W., S. Yueh, A. Fore, G. Neumann, A. Hayashi, and G. Lagerloef, "The rain effect on Aquarius' L-band sea surface brightness temperature and radar backscatter". *Remote Sensing of Environment*, 137, 147-157, 2013.
- [17] Reynolds, R. W., Smith, T. M., Liu, C., Chelton, D. B., Casey, K. S., & Schlax, M. G. , "Daily high-resolution blended analyses for sea surface temperature". *J. Climate*, 20, 5473-5496, 2007.
- [18] Chassignet, E. P., H.E. Hurlburt, E. J. Metzger, O. M. Smedstad, J. Cummings, G. R. Halliwell, R. Bleck, R. Baraille, A. J. Wallcraft, C. Lozano, H. L. Tolman, A. Srinivasan, A.

- Hankin, P. Cornillon, R. Weisberg, A. Barth, R. He, F. Werner, & J. Wilkin, “U.S. GODAE: Global Ocean Prediction with the HYbrid Coordinate Ocean Model (HYCOM)”. *Oceanography*, 22(2), 64-75, 2009.
- [19] Fore, A. G., S. H. Yueh, W. Tang, and A. K. Hayashi, “Aquarius Wind Speed Products: Algorithms and Validation”, *IEEE Trans. Remote Sens.*, Vol. PP, No.99, pp.1,8, 0. doi: 10.1109/TGRS.2013.2267616.
  - [20] Yueh, S., W. Tang, A. Fore, A. Hayashi and Y. T. Song, “Aquarius Geophysical Model Function and Combined Active Passive Algorithm for Ocean Surface Salinity and Wind Retrieval”. *J. Geophys. Res.-Oceans*, DOI: 10.1002/2014JC009939, 2014.
  - [21] Tang, W., S. H. Yueh, A. Fore, A. Hayashi, T. Lee, and G. Lagerloef, “Uncertainty of Aquarius sea surface salinity retrieved under rainy conditions and its implication on the water cycle study”. *J. Geophys. Res.-Oceans*, DOI: 10.1002/2014JC009834, 2014.
  - [22] Tang, W., S. H. Yueh, A. Fore, and A. Hayashi, “Validation of Aquarius sea surface salinity with in situ measurements from Argo floats and moored buoys”. *J. Geophys. Res.-Oceans*, DOI: 10.1002/2014JC010101, 2014.
  - [23] Yueh, S. H., W. Tang, A. G. Fore, and A. Hayashi, “Impact of Ocean Wave Height on L-band Passive and Active Microwave Observation of Sea Surfaces. The Special Issue of the IEEE Journal of Selected Topics in Applied Earth Observations and Remote Sensing (JSTARS) “Aquarius/SACD mission calibration/validation performance and retrieval algorithms”, (accepted) 2015.
  - [24] W. E. Asher, A. T. Jessup, R. Branch, and D. Clark, “Observations of rain-induced near-surface salinity anomalies”, *J. Geophys. Res. Oceans*, 119, doi: 10.1002/2014JC009954, 2014.
  - [25] A. Santos-Garcia, M. M. Jacob, W. L. Jones, W. E. Asher, Y. Hejazin, H. Ebrahimi, and M. Rabolli, “Investigation of rain effects on Aquarius sea surface salinity measurements”, *J. Geophys. Res. Oceans*, 119, 7605–7624, doi:10.1002/2014JC010137, 2014.
  - [26] Tang, W., S. H. Yueh, A. Hayashi, A. G. Fore, W. L. Jones, A. Santos-Garcia, and M. M. Jacob, “Rain-induced near surface salinity stratification and rain roughness correction for Aquarius SSS retrieval”. Submitted to The Special Issue of the IEEE Journal of Selected Topics in Applied Earth Observations and Remote Sensing (JSTARS) “Aquarius/SACD mission calibration/validation performance and retrieval algorithms”. (accepted) 2015.
  - [27] R. J. Joyce, J. E. Janowiak, P. A. Arkin, and P. Xie, “Cmorph: A method that produces global precipitation estimates from passive microwave and infrared data at high spatial and temporal resolution”, *Journal of Hydrometeorology*, 5, 487-503, doi:10.1175/1525-7541, 2004.
  - [28] P. Xie, R. Joyce, S. Wu, and F. Sun, “Reprocessed and bias-corrected CMORPH global high-resolution precipitation estimates for weather, climate, and hydrometeorological applications”. 7th International Precip Working Group (IPWG) Workshop, Nov. 17-20, 2014, Tsukuba, JAPAN, 2014.
  - [29] Roemmich, D., and the Argo Steering Team, “Argo: The challenge of continuing 10 years of progress”, *Oceanography*, 22, 46–55, 2009.
  - [30] McPhaden, M. J., The TAO array is completed. *Bull. Amer. Meteor. Soc.*, 76, 739–741, 1995.
  - [31] McPhaden and Coauthors (2009), RAMA: The Research Moored Array for African–Asian–Australian Monsoon Analysis and Prediction. *Bull. Amer. Meteor. Soc.*, 90, 459–480, 2009.

- [32] Servain, J., A. Busalacchi, M. McPhaden, A. Moura, G. Reverdin, M. Vienna, and S. Zebiak: “A Pilot Research Moored Array in the Tropical Atlantic (PIRATA)”. *Bull. Amer. Meteor. Soc.*, 79, 2019–2031, 1998.

#### IX. FIGURES AND CAPTIONS

Figure 1. The difference between (a)  $SSS_{CAP}$ , (b)  $SSS_{CAP\_RC}$  and APDRC Argo data for each month for the entire Aquarius mission from September 2011 to May 2015.

Figure 2. Time series of monthly biases (top) and RMS difference (bottom) for CAP (black) and CAP\_RC (red) with respect to Argo data between  $40^{\circ}S$  and  $40^{\circ}N$ , excluding two regions in the Eastern Pacific Fresh Pool and the Amazon River plume (as defined in [22]).

Figure 3. Daily time series of 30-days moving averaged buoy 1-m salinity (yellow),  $SSS_{CAP}$  (black),  $SSS_{CAP\_RC}$  (red),  $SSS_{HYCOM}$  (green) and APDRC Argo (blue) at TAO buoy location  $0^{\circ}N$ ,  $156^{\circ}E$  (a) and RAMA buoy location  $5^{\circ}S$ ,  $95^{\circ}E$  (b) where there are respectively 1263 and 988 buoy daily records for the period from September 1, 2011 to May 31, 2015.

Figure 4. At locations of the global tropical moored buoy arrays, the correlation coefficients (top), bias (middle) and RMS difference (bottom) between buoy 1-meter salinity and (a)  $SSS_{CAP}$ , (b)  $SSS_{CAP\_RC}$  based on all available daily records from Sept. 1, 2011 to May. 31, 2015 with 30 days moving average.

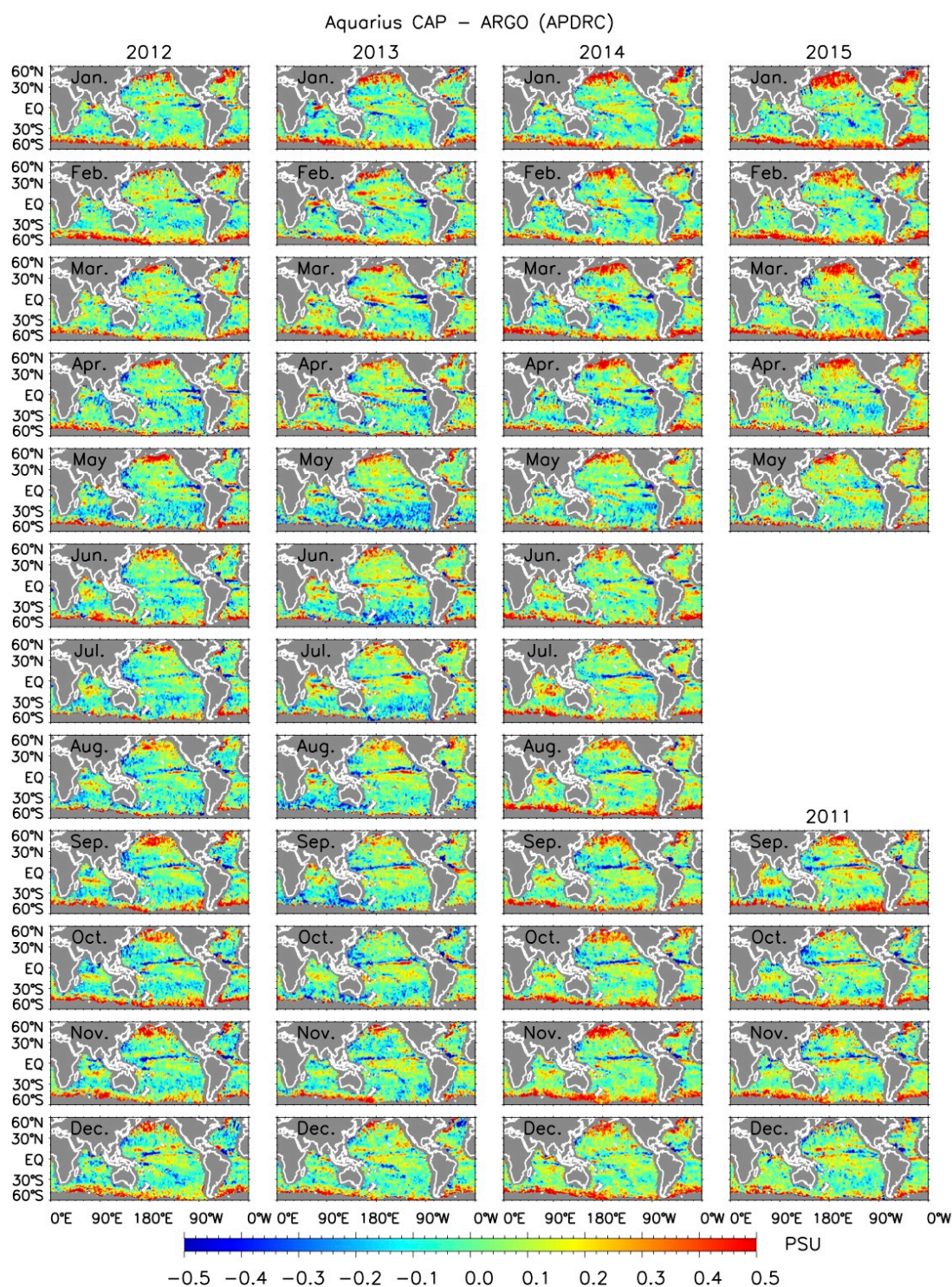


Figure 1. (a) The difference between  $SSS_{CAP}$  and APDRC Argo data for each month for the entire Aquarius mission from September 2011 to May 2015.



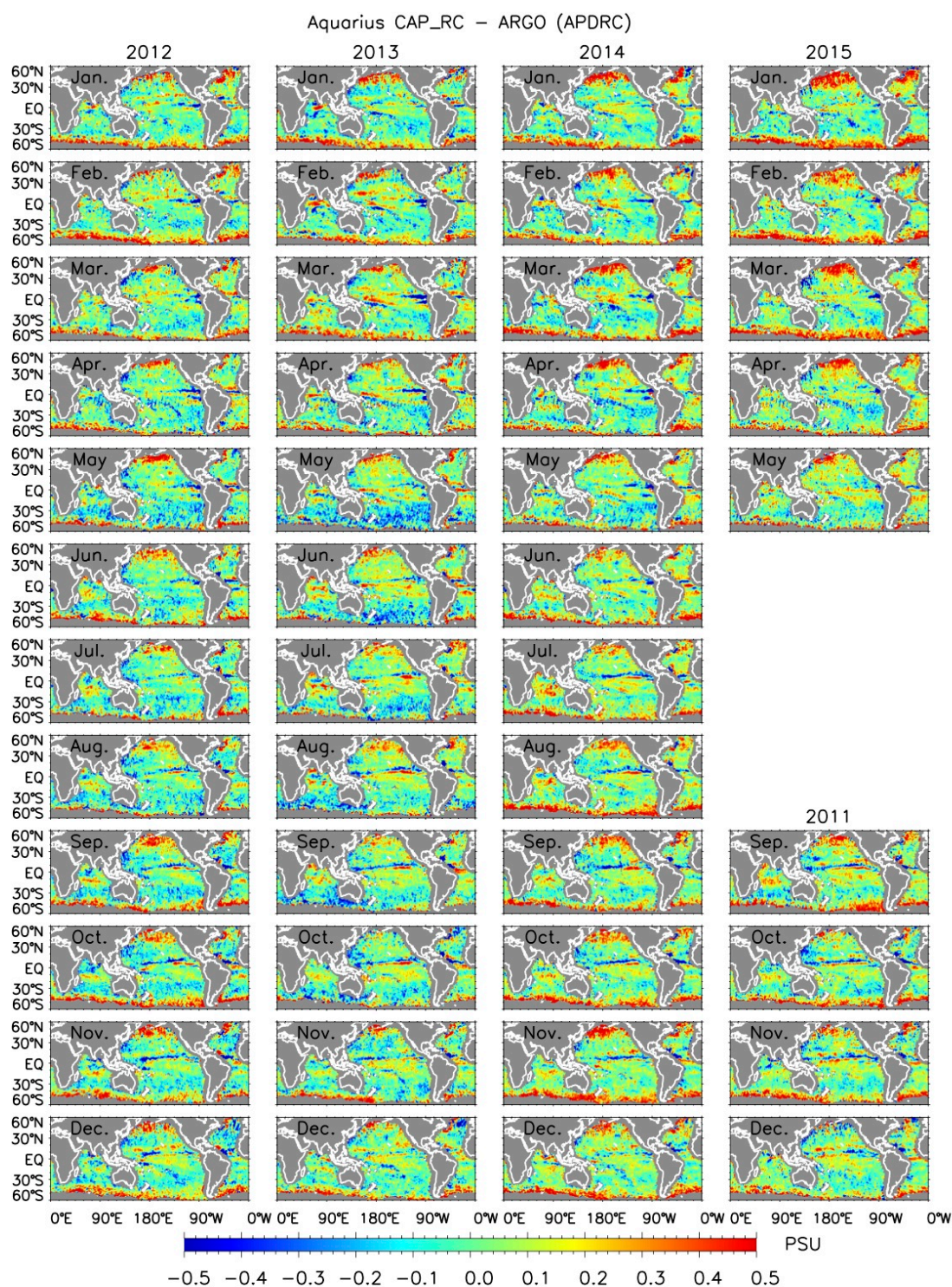


Figure 1. (b) Same as Fig.1a, for  $SSS_{CAP\_RC}$ .

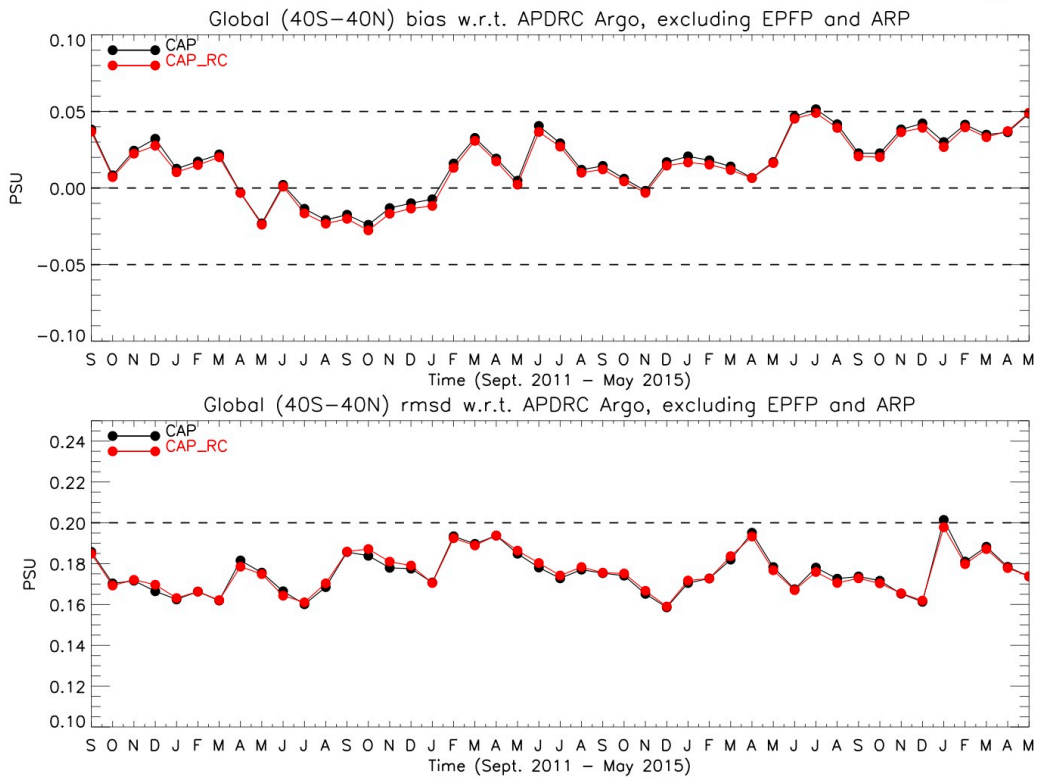
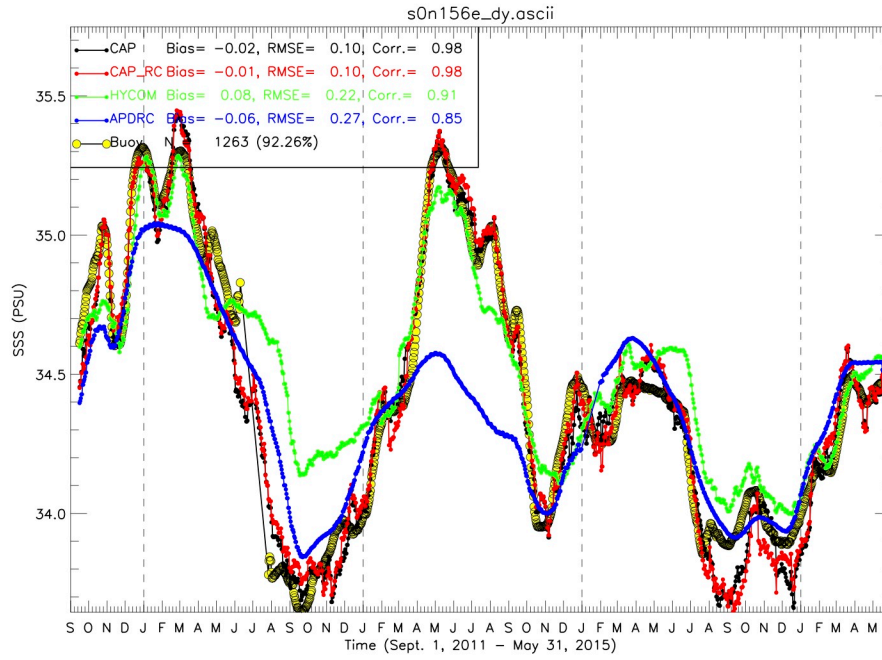


Figure 2. Time series of monthly biases (top) and RMS difference (bottom) for CAP (black) and CAP\_RC (red) with respect to Argo data between 40°S and 40°N, excluding two regions in the Eastern Pacific Fresh Pool and the Amazon River plume (as defined in [22]).

(a)



(b)

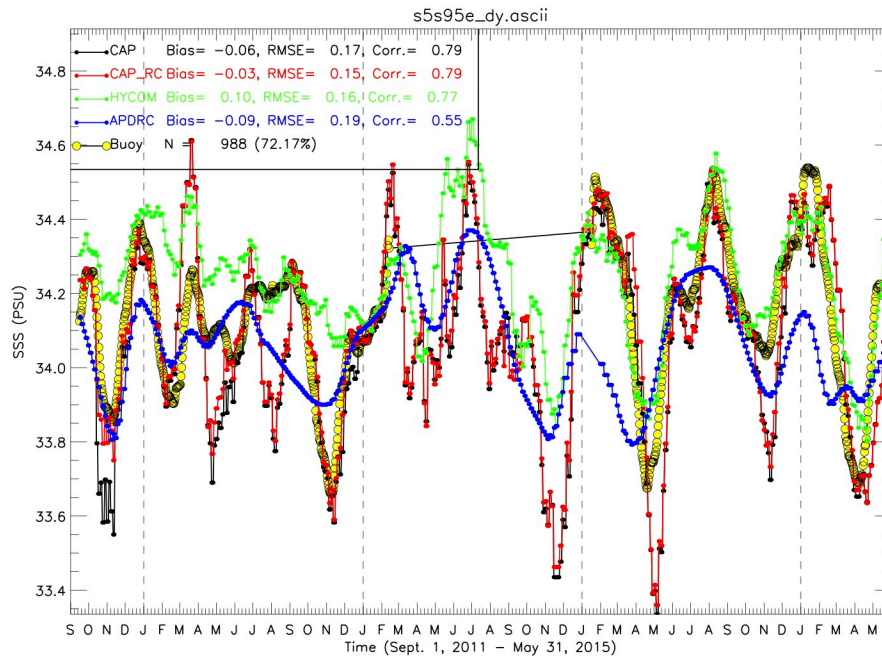


Figure 3. Daily time series of 30-days moving averaged buoy 1-m salinity (yellow),  $SSS_{CAP}$  (black),  $SSS_{CAP\_RC}$  (red),  $SSS_{HYCOM}$  (green) and APDRC Argo (blue) at TAO buoy location  $0^{\circ}N$ ,  $156^{\circ}E$  (a) and RAMA buoy location  $5^{\circ}S$ ,  $95^{\circ}E$  (b) where there are respectively 1263 and 988 buoy daily records for the period from September 1, 2011 to May 31, 2015.



(a)

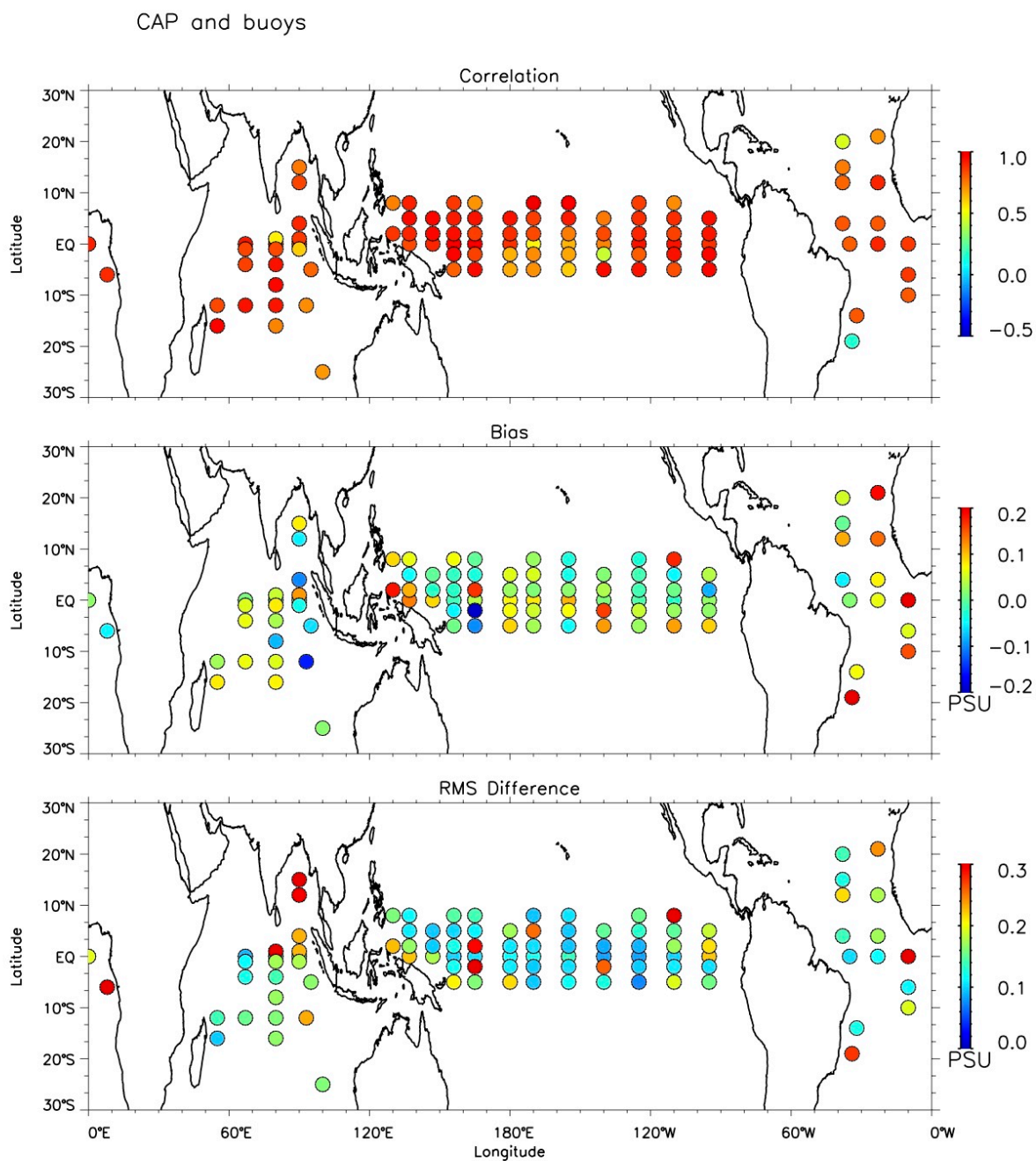


Figure 4. (a) At locations of the global tropical moored buoy arrays, the correlation coefficients (top), bias (middle) and RMS difference (bottom) between buoy 1-meter salinity and  $SSS_{CAP}$  based on all available daily records from Sept. 1, 2011 to May. 31, 2015 with 30 days moving average.



(b)

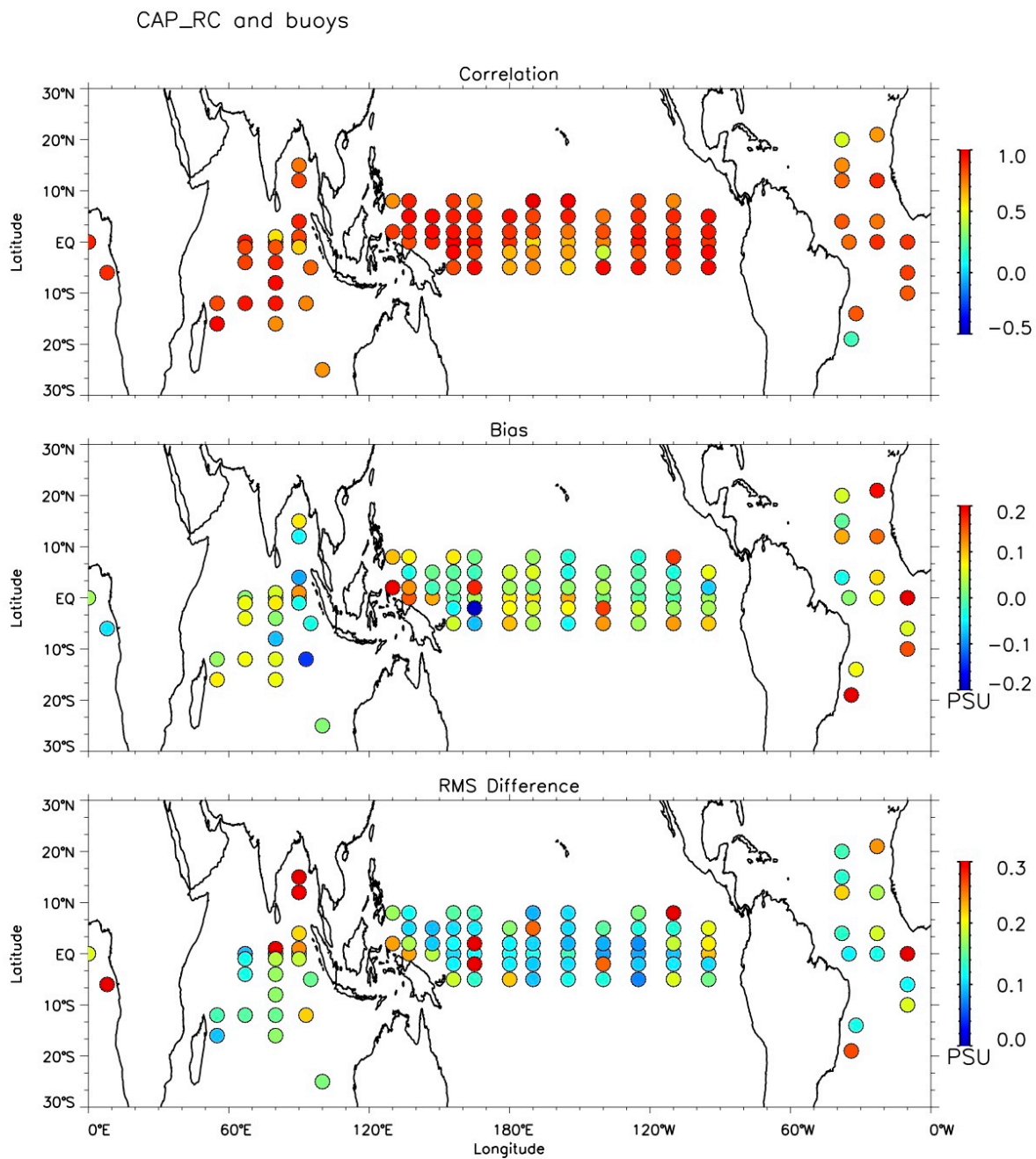


Figure 4. (b) Same as Fig. 4a, for  $SSS_{CAP\_RC}$ .

## X. APPENDIX

Time series plots of daily 1-m salinity observed by moored buoys compared with  $SSS_{CAP}$ ,  $SSS_{CAP\_RC}$ ,  $SSS_{HYCOM}$ , and APDRC Argo between September 1, 2011 and May 31, 2015, at each buoy location:

1. s0n0e
2. s0n10w
3. s0n110w
4. s0n125w
5. s0n137e
6. s0n140w
7. s0n147e
8. s0n155w
9. s0n156e
10. s0n165e
11. s0n170w
12. s0n180w
13. s0n23w
14. s0n35w
15. s0n67e
16. s0n90e
17. s0n95w
18. s10s10w
19. s12n23w
20. s12n38w
21. s12n90e
22. s12s55e
23. s12s67e
24. s12s93e
25. s14s32w
26. s15n38w
27. s15n90e
28. s16s55e
29. s19s34w
30. s20n38w
31. s21n23w
32. s25s100e
33. s2n110w
34. s2n125w
35. s2n130e
36. s2n137e

37. s2n140w  
38. s2n147e  
39. s2n155w  
40. s2n156e  
41. s2n165e  
42. s2n170w  
43. s2n180w  
44. s2n95w  
45. s2s110w  
46. s2s125w  
47. s2s140w  
48. s2s155w  
49. s2s156e  
50. s2s165e  
51. s2s170w  
52. s2s180w  
53. s2s95w  
54. s4n23w  
55. s4n38w  
56. s4n90e  
57. s4s67e  
58. s5n110w  
59. s5n125w  
60. s5n137e  
61. s5n140w  
62. s5n147e  
63. s5n155w  
64. s5n156e  
65. s5n165e  
66. s5n170w  
67. s5n180w  
68. s5n95w  
69. s5s110w  
70. s5s125w  
71. s5s140w  
72. s5s155w  
73. s5s156e  
74. s5s165e  
75. s5s170w  
76. s5s180w  
77. s5s95e  
78. s5s95w

- 79. s6s10w
- 80. s6s8e
- 81. s8n110w
- 82. s8n125w
- 83. s8n130e
- 84. s8n137e
- 85. s8n155w
- 86. s8n156e
- 87. s8n165e
- 88. s8n170w
- 89. s0n80.5e
- 90. s12s80.5e
- 91. s1.5n80.5e
- 92. s1.5n90e
- 93. s1.5s67e
- 94. s1.5s80.5e
- 95. s1.5s90e
- 96. s16s80.5e
- 97. s4s80.5e
- 98. s8s80.5e